RESEARCH ARTICLE

Doubly degenerate diffuse interface models of anisotropic surface diffusion

Marco Salvalaglio[1,2] | **Maximilian Selch**[1] | **Axel Voigt**[1,2] | **Steven M. Wise**[3]

[1]Institute of Scientific Computing, Department of Mathematics, TU Dresden, Dresden, Germany

[2]Dresden Center for Computational Materials Science, TU Dresden, Dresden, Germany

[3]Department of Mathematics, The University of Tennessee, Knoxville, Tennessee, USA

Correspondence
Marco Salvalaglio, Institute of Scientific Computing, Department of Mathematics, TU Dresden, 01062 Dresden, Germany.
Email: marco.salvalaglio@tu-dresden.de

Communicated by: X. Wang

We extend the doubly degenerate Cahn–Hilliard (DDCH) models for isotropic surface diffusion, which yield more accurate approximations than classical degenerate Cahn–Hilliard (DCH) models, to the anisotropic case. We consider both weak and strong anisotropies and demonstrate the capabilities of the approach for these cases numerically. The proposed model provides a variational and energy dissipative approach for anisotropic surface diffusion, enabling large-scale simulations with material-specific parameters.

KEYWORDS
anisotropy, degenerate Cahn–Hilliard equation, surface diffusion

MSC CLASSIFICATION
35Q56; 35K65; 65M60

1 | INTRODUCTION

Surface diffusion is an important transport mechanism in materials science, for example, in processes such as solid-state dewetting of semiconductors or coarsening of bulk nanoporous metals. In the isotropic setting, surface diffusion is modeled by a geometric evolution equation which relates the normal velocity of a hypersurface in Euclidean space to the surface Laplacian of the mean curvature,[1] for example, $v = \Delta_\Sigma H$. In more realistic anisotropic settings, the mean curvature is replaced by a weighted mean curvature, defined as the surface divergence of the Cahn–Hoffmann vector,[2] for example, $H_\gamma = \nabla_\Sigma \cdot D\gamma$, with $\gamma = \gamma(\hat{\mathbf{n}})$ an anisotropic surface energy and $\hat{\mathbf{n}}$ the outward-pointing surface normal. Even though some direct numerical approaches for these equations, in the isotropic and anisotropic setting exist—see, for example, other studies[3-8]—for most applications in materials science diffuse interface approximations are preferred—see, for example, previous studies.[9-20] These diffuse interface approaches capture the motion of the interface implicitly as the evolution of an isosurface of a phase-field function. Typically, they are fourth-order nonlinear diffusion equations of Cahn–Hilliard type, whose solutions formally converge to those of their sharp interface counterpart, as the interface thickness tends to zero.[12,21-23] They require a degenerate mobility function and are termed degenerate Cahn–Hilliard (DCH) equations. In

the model proposed in Wise et al,[12] an additional degeneracy is introduced, following similar ideas as used for the thin film limit in classical phase field models for solidification.[24] We call such models doubly degenerate Cahn–Hilliard (DDCH) models. This second degeneracy does not alter the asymptotic limit[12] but actually leads to more accurate surface diffusion approximations. See, for example, the discussion in Backofen et al.[25] In fact, several simulations for realistic applications in materials science consider this model—see, for example, other studies[26-38]—and claim that their large-scale simulations would not be feasible without the additional degeneracy. The drawback of this DDCH model, which is termed *RRV model* in several publications,[22,31,36] is that it is nonvariational. That is, there is no known free energy that is dissipated along solution trajectories. This makes it harder to prove properties of solutions and derive certain numerical stabilities. In Salvalaglio et al,[39] this problem was solved by introducing a new variational DDCH model for surface diffusion, which can be connected with the nonvariational DDCH model of Rätz et al.[12] This was done for the isotropic case and will here be generalized to the anisotropic case.

The paper is organized as follows: in Section 2, we first review the different isotropic DDCH models, their connection, and then extend the idea to weak as well as strong anisotropies. The latter case requires an additional curvature regularization, leading to higher order equations; in Section 3, we illustrate the numerical approach which uses a semi-implicit time-integration scheme and adaptive finite elements for discretization in space; two- and three-dimensional numerical results are shown in Section 4, including comparisons between different models and with sharp-interface solutions. Different choices for surface-energy densities are reported, also matching real material properties, and applications are illustrated to show the wide applicability. In Section 5, we draw our conclusions.

2 | MODELS

2.1 | Isotropic, variational DDCH model

Suppose that $\Omega \subset \mathbb{R}^d$, $d = 2, 3$, is a bounded, open set. Let us consider the free energy

$$F[u] = \int_\Omega g_0(u) \left(\frac{1}{\epsilon} f(u) + \frac{\epsilon}{2} |\nabla u|^2 \right) d\mathbf{x}, \tag{1}$$

with $f = \frac{\omega}{4} u^2 (1-u)^2$, $\omega = 72$ a quartic, symmetric double well potential and g_0 a singular function of the form

$$g_0(u) = \frac{1}{\xi |u|^p |1-u|^p}, \ p \geq 0, \ \xi > 0.$$

g_0 can be regularized so that it is defined, continuous, and differentiable for all u:

$$g_\alpha(u) = \frac{1}{\sqrt{\xi^2 (u^2(1-u)^2)^p + \alpha^2 \epsilon^2}}, \ p \geq 0, \ \xi > 0, \ \alpha \geq 0.$$

The dynamics is described as the H^{-1} gradient flow by

$$\partial_t u = \frac{1}{\epsilon} \nabla \cdot (M_0(u) \nabla w), \tag{2}$$

$$w = g_0'(u) \left(\frac{\epsilon}{2} |\nabla u|^2 + \frac{1}{\epsilon} f(u) \right) + g_0(u) \frac{1}{\epsilon} f'(u) - \epsilon \nabla \cdot (g_0(u) \nabla u), \tag{3}$$

where $w = \delta_u F$ is the chemical potential with $\delta_u F$ the variational derivative of the free energy F with respect to u. M_0 is the degenerate mobility function. Its regularized form is

$$M_\alpha(u) = \mu u^2 (1-u)^2 + \alpha \epsilon, \ \mu = 36, \ \alpha \geq 0, \tag{4}$$

and M_0 is obtained setting $\alpha = 0$.

In Salvalaglio et al,[39] it is shown that Equations (2) and (3) formally converge to motion by surface diffusion if $\epsilon \to 0$, $0 \leq p < 2$ and $\xi = 6 \frac{\Gamma(2-p))^2}{\Gamma(4-2p)}$ with Γ the usual (Bernoulli) Gamma-function. The proposed system, Equations (2) and (3), is a free energy dissipative dynamical system.

With the asymptotic approximation $\frac{1}{\varepsilon}f(u) \approx \frac{\varepsilon}{2}|\nabla u|^2$—which holds when the interface has a hyperbolic tangent profile—we obtain $w \approx g_0(u)\frac{1}{\varepsilon}f'(u) - \varepsilon g_0(u)\nabla^2 u$, which simplifies Equation (3) and leads to

$$\partial_t u = \frac{1}{\varepsilon}\nabla \cdot (M_0(u)\nabla w),\tag{5}$$

$$\xi|u|^p|1-u|^p w = \frac{1}{\varepsilon}f'(u) - \varepsilon\nabla^2 u.\tag{6}$$

This model is strikingly similar to the isotropic version of the model in Rätz et al,[12] but with one important caveat. The model in Rätz et al[12] corresponds to the choice $p = 2$, which is not defined for Equations (2)–(3).[39] Interestingly, Equations (5)–(6) can be defined in a reasonable way for any $p \in [0,\infty)$. The choice of ξ will not be the same as for Equations (2)–(3), in general. However, for $p = 1$, they are identical. See Salvalaglio et al[39] for details.

Numerical solutions indicate a higher accuracy for the variational DDCH model Equations (2) and (3) and the non-variational DDCH model Equations (5) and (6) if compared with the classical DCH model ($p = 0$ and $\xi = 1$). Another advantage of the DDCH models is that deviations of u from the pure phase values, 0 and 1, are smaller in a point-wise sense, when compared with the solutions of the classical DCH model. This property can further be elaborated to guarantee, in the nonregularized case $\alpha = 0$, that $0 \le u \le 1$ for DDCH approximations. So-called positivity preserving schemes of the variational DDCH model, Equations (2) and (3), are possible and will be discussed in later publications.

2.2 | Anisotropic, variational DDCH model

Instead of a constant surface-energy density $\gamma = 1$, most materials have anisotropic surface-energy density $\gamma = \gamma(\hat{\mathbf{n}})$. In the phase-field context, γ is extended by defining $\hat{\mathbf{n}}^0 = -\frac{\nabla u}{|\nabla u|}$. In other words, γ is defined everywhere that $\nabla u \neq \mathbf{0}$. We consider the free energy given by

$$F[u] = \int_\Omega \gamma(\hat{\mathbf{n}}^0)g_0(u)\left(\frac{1}{\varepsilon}f(u) + \frac{\varepsilon}{2}|\nabla u|^2\right)d\mathbf{x}.\tag{7}$$

In contrast to classical approach of Kobayashi,[40] in which the anisotropic surface-energy density only affects gradient term of the free energy—see, for example, other studies [6,9-11,41,42] for stable numerical realizations and even numerical convergence theory[9]—we here follow the approach of Torabi et al,[14] which ensures that the interface thickness is independent of orientation. As in Salvalaglio et al,[39] we include the energy restriction function g_0, which is singular at the pure phase values $u = 0, 1$. The asymptotic analysis of Salvalaglio et al[39] can be repeated, under the assumption that the diffuse interface has the usual hyperbolic tangent profile, to show that $F[u] \approx \int_\Sigma \gamma(\hat{\mathbf{n}}(s))\,ds$, where $\Sigma = \{\mathbf{x} \in \Omega \mid u(\mathbf{x}) = 0.5\}$ and $\hat{\mathbf{n}}(s)$ is normal for Σ.

2.2.1 | Model regularization

We note that Equation (7) is not defined for arbitrary smooth functions u. This can be an enormous problem for practical computations. To fix this, we regularize the energy as follows. Set $\mathbf{p} = \nabla u$. Define the regularized, extended normal

$$\hat{\mathbf{n}}^\alpha := \frac{-\mathbf{p}}{\sqrt{|\mathbf{p}|^2 + \alpha^2\varepsilon^2}},$$

and observe that this vector is now (i) only approximately of unit length and (ii) only approximately normal to the level sets of u. The regularized free energy is defined as

$$F_\alpha[u] = \int_\Omega \gamma(\hat{\mathbf{n}}^\alpha)g_\alpha(u)\left(\frac{1}{\varepsilon}f(u) + \frac{\varepsilon}{2}|\nabla u|^2\right)d\mathbf{x},\tag{8}$$

which is now well-defined for arbitrary smooth phase-field functions. We note that it is possible, and perhaps even advantageous in some settings, to use two separate regularization parameters for $\hat{\mathbf{n}}^0$ and g_0, but we will avoid this technical discussion here and instead focus on formulation and numerics.

In the computation of the variational derivative of F_α, denoted $\delta_u F_\alpha$, we need the following calculation:

$$\left[\nabla_\mathbf{p} \gamma(\hat{\mathbf{n}}^\alpha)\right]_i = \frac{\partial \gamma(\hat{\mathbf{n}}^\alpha)}{\partial p_i} = \sum_{j=1}^{d} P_{i,j}^\alpha \frac{\partial \gamma(\hat{\mathbf{n}}^\alpha)}{\partial n_j^\alpha} = \left[\mathbf{P}^\alpha \nabla_{\hat{\mathbf{n}}^\alpha} \gamma(\hat{\mathbf{n}}^\alpha)\right]_i,$$

where

$$\left[\mathbf{P}^\alpha\right]_{i,j} = P_{i,j}^\alpha := \frac{\partial n_j^\alpha}{\partial p_i} = -\frac{\delta_{i,j} - n_i^\alpha n_j^\alpha}{\sqrt{|\mathbf{p}|^2 + \alpha^2 \varepsilon^2}} = -\frac{[\mathbf{I} - \mathbf{n}^\alpha \otimes \mathbf{n}^\alpha]_{i,j}}{\sqrt{|\mathbf{p}|^2 + \alpha^2 \varepsilon^2}},$$

a regularized projection-like matrix. The regularized doubly degenerate energy dissipative flow now reads

$$\partial_t u = \frac{1}{\varepsilon} \nabla \cdot (M_\alpha(u) \nabla w), \tag{9}$$

$$w = \gamma(\hat{\mathbf{n}}^\alpha) \left(g_\alpha'(u) \left(\frac{\varepsilon}{2} |\nabla u|^2 + \frac{1}{\varepsilon} f(u) \right) + g_\alpha(u) \frac{1}{\varepsilon} f'(u) \right) - \nabla \cdot \left(\nabla_\mathbf{p} \gamma(\hat{\mathbf{n}}^\alpha) g_\alpha(u) \left(\frac{\varepsilon}{2} |\nabla u|^2 + \frac{1}{\varepsilon} f(u) \right) + \gamma(\hat{\mathbf{n}}^\alpha) g_\alpha(u) \varepsilon \nabla u \right), \tag{10}$$

where $w = \delta_u F_\alpha$ is the chemical potential. We point out that the chemical potential becomes singular and ill-defined when the regularization is formally turned off ($\alpha = 0$), in particular, when $\nabla u = \mathbf{p} = \mathbf{0}$, $u = 0$, or $u = 1$.

2.2.2 | Strong anisotropy

Equations (9) and (10) can only be well-posed as long as the graph of $\gamma(\hat{\mathbf{n}})$ is convex, corresponding to so-called weak anisotropies. Strong anisotropies, which also allow for facets, require a corner regularization. We follow Torabi et al[14] and add a diffuse Willmore-type regularization. The free energy reads

$$F_\alpha[u] = \int_\Omega \left\{ \gamma(\hat{\mathbf{n}}^\alpha) g_\alpha(u) \left(\frac{1}{\varepsilon} f(u) + \frac{\varepsilon}{2} |\nabla u|^2 \right) + \frac{\beta}{2\varepsilon} \left(-\varepsilon \nabla^2 u + \frac{1}{\varepsilon} f'(u) \right)^2 \right\} d\mathbf{x}, \tag{11}$$

with $\beta > 0$. Physically, $\beta^{1/2}$ defines a length scale over which corners and edges are smeared out—see Torabi et al[14] and Gurtin and Jabbour.[43] The considered diffuse interface approximation of the Willmore energy follows from the proposed form in De Giorgi[44] by using the asymptotic approximation $\frac{1}{\varepsilon} f(u) \approx \frac{\varepsilon}{2} |\nabla u|^2$. See previous studies.[45-47] The energy dissipative flow reads

$$\partial_t u = \frac{1}{\varepsilon} \nabla \cdot (M_\alpha(u) \nabla w), \tag{12}$$

$$w = \gamma(\hat{\mathbf{n}}^\alpha) \left(g_\alpha'(u) \left(\frac{\varepsilon}{2} |\nabla u|^2 + \frac{1}{\varepsilon} f(u) \right) + g_\alpha(u) \frac{1}{\varepsilon} f'(u) \right) - \nabla \cdot \left(\nabla_\mathbf{p} \gamma(\hat{\mathbf{n}}^\alpha) g_\alpha(u) \left(\frac{\varepsilon}{2} |\nabla u|^2 + \frac{1}{\varepsilon} f(u) \right) + \gamma(\hat{\mathbf{n}}^\alpha) g_\alpha(u) \varepsilon \nabla u \right)$$
$$+ \beta \left(\frac{1}{\varepsilon^2} f''(u) \kappa - \nabla^2 \kappa \right), \tag{13}$$

$$\kappa = -\varepsilon \nabla^2 u + \frac{1}{\varepsilon} f'(u). \tag{14}$$

We remark that using a *low-order* mobility function—such as $M_0(u) = Cu(1 - u)$ which was employed in Torabi et al[14]—solutions would not actually converge to motion by anisotropic surface diffusion, as $\epsilon \to 0$. The reasons are laid out in other studies.[48-50] However, the asymptotic analysis with $M_0(u)$ as in Equation (4) leads to the desired results for both models (9)–(10) and (13)–(14), provided $g_0 = 1$, as shown in previous studies.[12,22,51] Additionally, combining these results with the results of Salvalaglio et al[39] will give the same asymptotic limits as $\epsilon \to 0$ for the doubly degenerate cases with $g_0(u)$. The limiting model reads $v = \Delta_\Sigma \left(H_\gamma + \beta \left(\Delta_\Sigma H + \frac{1}{2} H^3 - 2HK \right) \right)$, with Gaussian curvature K—see, for example, Gurtin and Jabbour.[43]

Also for the anisotropic cases, the asymptotic approximation $\frac{1}{\varepsilon} f(u) \approx \frac{\varepsilon}{2} |\nabla u|^2$ can be used to simplify the equations and, in turn, their numerical integration. However, a one-to-one correspondence with the nonvariational models proposed in Rätz et al[12] is not possible. The corresponding version, including the surface-energy density as in Torabi et al,[14] reads

$$\partial_t u = \frac{1}{\varepsilon} \nabla \cdot (M_0(u) \nabla w), \tag{15}$$

$$\xi|u|^p|1-u|^p w = -\varepsilon\nabla\left(\gamma(\hat{\mathbf{n}}^0)\nabla u\right) + \frac{1}{\varepsilon}\gamma(\hat{\mathbf{n}}^0)f'(u) - \varepsilon\nabla\cdot\left(|\nabla u|^2\nabla_{\mathbf{p}}\gamma(\hat{\mathbf{n}}^0)\right) + \beta\left(\frac{1}{\varepsilon^2}f''(u)\kappa - \nabla^2\kappa\right), \tag{16}$$

$$\kappa = -\varepsilon\Delta u + \frac{1}{\varepsilon}f'(u), \tag{17}$$

with $p = 1$, $\xi = 6$ or $p = 2$, $\xi = 30$, and $\beta = 0$ for weak and $\beta > 0$ for strong anisotropy. Also, these models formally converge asymptotically to the expected anisotropic surface diffusion models as $\varepsilon \to 0$ and have been frequently used in applications—see, for example, other studies.[18,19,35] To be practically useful, also Equations (15)–(17) require an appropriate regularization.[12] In the following, we will refer to Equations (15)–(17) as the *RRV model*.

3 | NUMERICS

Our goal is to demonstrate the advantageous solution properties of the DDCH models, as well as to show that the variational DDCH models are suitable for simulating the formation of complex faceted morphologies. We will in the following consider the case $p = 1$ and $\xi = 6$ for the variational model (12)–(14). The classical DCH model can be straightforwardly considered by setting $p = 0$ and $\xi = 1$. (Thus, we can take $g_\alpha \equiv 1$). For the time-integration of the *RRV model*, we refer to Rätz et al[12] and Torabi et al.[14] We employ the regularized functions $\hat{\mathbf{n}}^\alpha$, g_α, and M_α using the value $\alpha = 10^{-6}$.

We solve the models using adaptive finite elements, implemented in the software package AMDiS.[52,53] The time-integration scheme is semi-implicit and follows the scheme employed for the isotropic case,[39] which reads,

$$\frac{u^{n+1}}{\tau_n} - \frac{1}{\varepsilon}\nabla\cdot\left(M_\alpha(u^n)\nabla w^{n+1}\right) = \frac{u^n}{\tau_n}, \tag{18}$$

$$w^{n+1} + \varepsilon\nabla\cdot\left[g_\alpha(u^n)\nabla u^{n+1}\right] - \frac{1}{\varepsilon}\left[r(u^n) + s(u^n)\right]u^{n+1} + \frac{\varepsilon}{2}g_\alpha'(u^n)\nabla u^n\cdot\nabla u^{n+1} = q(u^n), \tag{19}$$

where

$$q(u^n) = \frac{1}{\varepsilon}g_\alpha(u^n)f'(u^n) + \frac{1}{\varepsilon}g_\alpha'(u^n)f(u^n) - \frac{1}{\varepsilon}\left[r(u^n) + s(u^n)\right]u^n,$$
$$r(u^n) = \left[g_\alpha'(u^n)f'(u^n) + g_\alpha(u^n)f''(u^n)\right],$$
$$s(u^n) = \left[g_\alpha'(u^n)f'(u^n) + g_\alpha''(u^n)f(u^n)\right],$$

account for the linearizations of $g_\alpha(u^{n+1})f'(u^{n+1})$ and $g\alpha'(u^{n+1})f(u^{n+1})$ around u^n. The integer n is the time step index, τ_n the time stepsize at step n, and u^0 the initial condition.

To employ this scheme for the anisotropic cases, $\gamma(\hat{\mathbf{n}}^\alpha)$ has to be included. The scheme for the variational model (12)–(14) reads

$$\frac{u^{n+1}}{\tau_n} - \frac{1}{\varepsilon}\nabla\cdot\left[M_\alpha(u^n)\nabla w^{n+1}\right] = \frac{u^n}{\tau_n}, \tag{20}$$

$$w^{n+1} + \varepsilon\nabla\cdot\left(\gamma_\alpha^n g_\alpha(u^n)\nabla u^{n+1}\right) - \gamma_\alpha^n\frac{1}{\varepsilon}\left[r(\varphi^n) + s(\varphi^n)\right]u^{n+1}$$
$$+ \frac{\varepsilon}{2}\gamma_\alpha^n g_\alpha'(u^n)\nabla u^n\cdot\nabla u^{n+1} + \beta\left(-\frac{1}{\varepsilon^2}f'(u^n)\kappa^{n+1} + \nabla^2\kappa^{n+1}\right) = \gamma_\alpha^n q(u^n) + A(u^n), \tag{21}$$

$$\kappa^{n+1} + \varepsilon\nabla^2 u^{n+1} - \frac{1}{\varepsilon}f'(u^n)u^{n+1} = \frac{1}{\varepsilon}f'(u^n) - \frac{1}{\varepsilon}f''(u^n)u^n, \tag{22}$$

where

$$\gamma_\alpha^n := \gamma\left(\hat{\mathbf{n}}^{\alpha,n}\right),\ \hat{\mathbf{n}}^{\alpha,n} := -\frac{\mathbf{p}^n}{\sqrt{|\mathbf{p}^n|^2 + \alpha^2\varepsilon^2}},\ \mathbf{p}^n := \nabla u^n,$$

$$A(u^n) := -\nabla\cdot\left(g_\alpha(u^n)\mathbf{P}^{\alpha,n}\nabla_{\hat{\mathbf{n}}^\alpha}\gamma(\hat{\mathbf{n}}^{\alpha,n})\left(\frac{\varepsilon}{2}|\nabla u^n|^2 + \frac{1}{\varepsilon}f(u^n)\right)\right),\ \text{and}\ \left[\mathbf{P}^{\alpha,n}\right]_{i,j} = P_{i,j}^{\alpha,n} := -\frac{\delta_{i,j} - n_i^{\alpha,n}n_j^{\alpha,n}}{\sqrt{|\mathbf{p}^n|^2 + \alpha^2\varepsilon^2}}. \tag{23}$$

For weak anisotropies, we set $\beta = 0$, and Equation (22) is not needed. The system is discretized in space by piecewise linear finite elements. We consider simplicial meshes which are adaptively refined by bisection to ensure a resolution ranging between $5h \sim \varepsilon$ and $10h \sim \varepsilon$, with mesh size h, within the diffuse interface. The resulting linear system is solved by an iterative solver exploiting the biconjugate gradient stabilized method (BiCGstab(l)),[54] with a block Jacobi preconditioner (bjacobi) applied to the blocks resulting from an element-wise domain decomposition, with a local sparse direct solver UMFPACK.[55]

Remark 1. Since we employ the regularized models in our numerical experiments, the positivity of u, namely, $0 < u < 1$, is neither expected to hold, nor required to hold, in the numerical results. However, as the regularization parameter is decreased, the degree of the overshoots—that is, u going above 1 and/or below 0—are reduced. We have confirmed this in numerical tests not reported here. A comparison of overshoots in the various models is graphically illustrated in Figure 2. The design of a theoretically positivity preserving and energy dissipating numerical scheme for the present anisotropic variational model would be a difficult undertaking, in our experience. However, it is possible to develop such a scheme for the isotropic variational DDCH model, and we plan to give the details of that in a future paper.

4 | NUMERICAL RESULTS

Numerical results are chosen to demonstrate the advantageous solution properties and possibilities of the variational DDCH model for applications in materials science. We compare the variational DDCH model with the *RRV model* and the classical DCH model for various anisotropies in 2D. The chosen examples in 3D show faceting with material-specific anisotropies and large-scale coarsening simulations in nanoporous materials.

In 2D, we consider a simple, fourfold anisotropy

$$\gamma_4(\hat{\mathbf{n}}) = 1 + C \left(4 \left(n_x^4 + n_y^4 \right) - 3 \right),$$

which in polar form is

$$\gamma_4(\hat{\mathbf{n}}) = \tilde{\gamma}_4(\theta) = 1 + C \cos(4\theta), \ \theta = \text{atan} \left(\frac{n_y}{n_x} \right). \tag{24}$$

With this choice, $\gamma(\hat{\mathbf{n}})$ is convex (weakly anisotropy) for values $C < \frac{1}{15}$ and nonconvex (strongly anisotropy) for $C > \frac{1}{15}$. The evolution obtained with Equations (9)–(10) or Equations (13)–(14), depending on C, is illustrated in Figure 1. The initial setting is a 2D shape with varying positive and negative curvatures as in Salvalaglio et al.[39] The final shape, the obtained equilibrium configuration, is the approximation of the corresponding Wulff shape, with facets and rounded corners for the nonconvex (strongly anisotropic) free energy. For both cases, the evolution can also be obtained with the RRV and DCH models. (Recall that the DCH model is obtained from the DDCH model using $g_\alpha \equiv 1$.) Visually, there is no difference. However, as already discussed for the isotropic case, the variational DDCH model has better "positivity"

FIGURE 1 Evolution obtained by the anisotropic variational doubly degenerate Cahn–Hilliard (DDCH) model ($\varepsilon = 0.2$). The shapes are obtained as white-to-black color maps for $|\nabla u|^2$. Different shapes (left to right) correspond to time 0τ, $10^2\tau$, $5 \cdot 10^2\tau$, $15 \cdot 10^2\tau$, $30 \cdot 10^2\tau$, $60 \cdot 10^2\tau$ with $\tau = 2 \cdot 10^{-5}$ the timestep for weak anisotropy and $\tau = 1 \cdot 10^{-5}$ the timestep for strong anisotropy. The first shape on the left corresponds to the initial condition; it shows also the adaptive computational mesh and the bounds of the computational domain with size 2×2. The last shapes on the right are the reached equilibrium shapes. Anisotropic surface energy is set as in Equation (24) with parameters as specified in the figure. The solutions are independent to further mesh refinement [Colour figure can be viewed at wileyonlinelibrary.com]
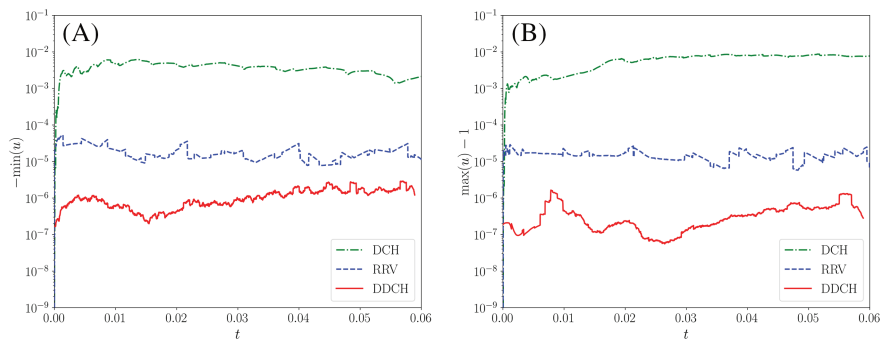

WEAK C=1/16

STRONG C=1/3 β=0.025

TIME
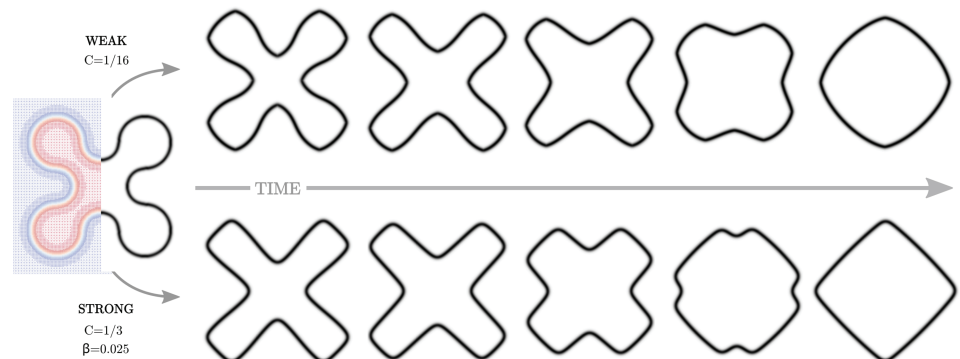
FIGURE 2 The minimum and maximum of u for the simulation in Figure 1 (weak anisotropy) is shown by means of $-\min(u)$ (A) and $\max(u) - 1$ (B), respectively, for (i) the standard degenerate Cahn–Hilliard model (DCH, green dashed-dotted line), (ii) the RRV model (dashed blue line), and (iii) the variational doubly degenerate Cahn–Hilliard model Equations (9) and (10) (DDCH, red solid line) [Colour figure can be viewed at wileyonlinelibrary.com]

properties. Note, however, that since we are using a regularized model, and since our numerical method is not designed for positivity, the numerical approximations of the DDCH model do not preserve the positivity property $0 < u < 1$ precisely. However, the overshoot values are very small for the DDCH and RRV models. The DDCH model performs the best, as the overshoots are closer to the pure phase values $u = 0$ and $u = 1$.

Clear evidence of this aspect in the anisotropic case is reported in Figure 2. It shows the deviation from the nominal values of u, namely, 0 and 1, away from the interface through $-\min(u)$ and $\max(u) - 1$, respectively. The variational DDCH model shows values, which are between one and two orders of magnitudes closer to the nominal values (0 in both plots) with respect to the *RRV model* and three to four orders of magnitude closer with respect to the DCH model. It is worth mentioning that these values depend on the specific simulation set up. However, we expect the relative difference between the models to hold true generally.

The better approximation properties of the variational DDCH and RRV models, if compared with the classical DCH model in the isotropic case, have already been shown in Backofen et al[25] and Salvalaglio et al,[39] respectively. These properties result in the possibility to use larger ϵ and thus lower grid resolution, to reach the same accuracy, which enables the large-scale simulations in various applications. In the anisotropic setting, the differences between the variational DDCH and RRV models and the classical DCH model become even more severe and might lead to divergence of the DCH model for strong anisotropies and desired error tolerances. To demonstrate this, we compare the reached equilibrium shape with the desired Wulff shape of the sharp interface problem. We closely follow convergence studies considered in Haußer and Voigt[4] for a sharp interface model for strongly anisotropic surface diffusion. Figure 3A–C shows the evolution from a circle with radius = 5 towards the equilibrium shape for different β. We consider $\epsilon = 0.6$ and $\gamma(\hat{\mathbf{n}})$ as in Equation (24) with $C = \frac{1}{2}$. Focusing on the rounded upper corner of the desired Wulff shape allows to construct an asymptotic solution for the limiting sharp interface problem, see Spencer[56] for details. Briefly, the idea is to take the sharp corner equilibrium shape ($\beta = 0$) as the outer solution and to derive an inner solution for the equilibrium shape near the corner as an expansion in $\beta^{1/2}$. Let s be the arclength with $s = 0$ at the corner of the outer solution and $\Theta(S) = \theta\left(s/\beta^{1/2}\right)$ the rescaled local orientation. Expanding $\Theta(S) = \Theta_0(S) + \beta^{1/2}\Theta_1(S) + \dots$, one obtains the lowest order term $\Theta_0(S)$ by inverting

$$S(\Theta_0) = \int_0^{\Theta_0} \frac{1}{\sqrt{2Q(\Theta')}} d\Theta' \quad \text{with} \quad Q(\Theta_0) = \gamma(\Theta_0) + A\cos(\Theta_0), \tag{25}$$

with $A = -\gamma(\theta_c)\cos(\theta_c) + \gamma'(\theta_c)\sin(\theta_c)$ and $\theta_c = \pm\frac{\pi}{4}$ the corner orientation of the outer solution. The composite solution in the neighborhood of a corner with inner solution θ_{inner} is then given by $\theta(s) = \theta_{\text{inner}}(s) + \theta_{\text{outer}}(s) - \theta_{\text{match}}$, with $\theta_{\text{match}} = \pm\frac{\pi}{4}$, with the sign depending on the sign of s. Figure 3D,E shows the solution for various β in an (x, y)- and (s, θ)-plot, respectively. The comparison of our numerical solutions of the variational DDCH, RRV, and DCH models for fixed ϵ with these asymptotic solutions is shown in Figure 3F,G, for $\beta = 1$ and $\beta = 0.25$, respectively. Two spatial discretizations are shown corresponding to 5 ($h = 0.12$ and 10 ($h = 0.06$) grid points across the diffuse interface, demonstrating the good approximation properties of the double degenerate models already for moderate values of ϵ.

For examples in 3D with strong anisotropy, we consider $\gamma(\hat{\mathbf{n}})$ as proposed in Salvalaglio et al[18]:

$$\gamma(\hat{\mathbf{n}}) = \gamma_0 \left[1 - \sum_i^N \rho_i(\hat{\mathbf{n}} \cdot \mathbf{m}_i)^{\omega_i} \Theta(\hat{\mathbf{n}} \cdot \mathbf{m}_i) \right], \tag{26}$$

with $\mathbf{m}_i$ the normals to the surface corresponding to minima of $\gamma(\hat{\mathbf{n}})$, ρ_i the depth of energy minima, ω_i controlling the extension of energy well around $\mathbf{m}_i$ and N the total number of different minima. This particular form provides the
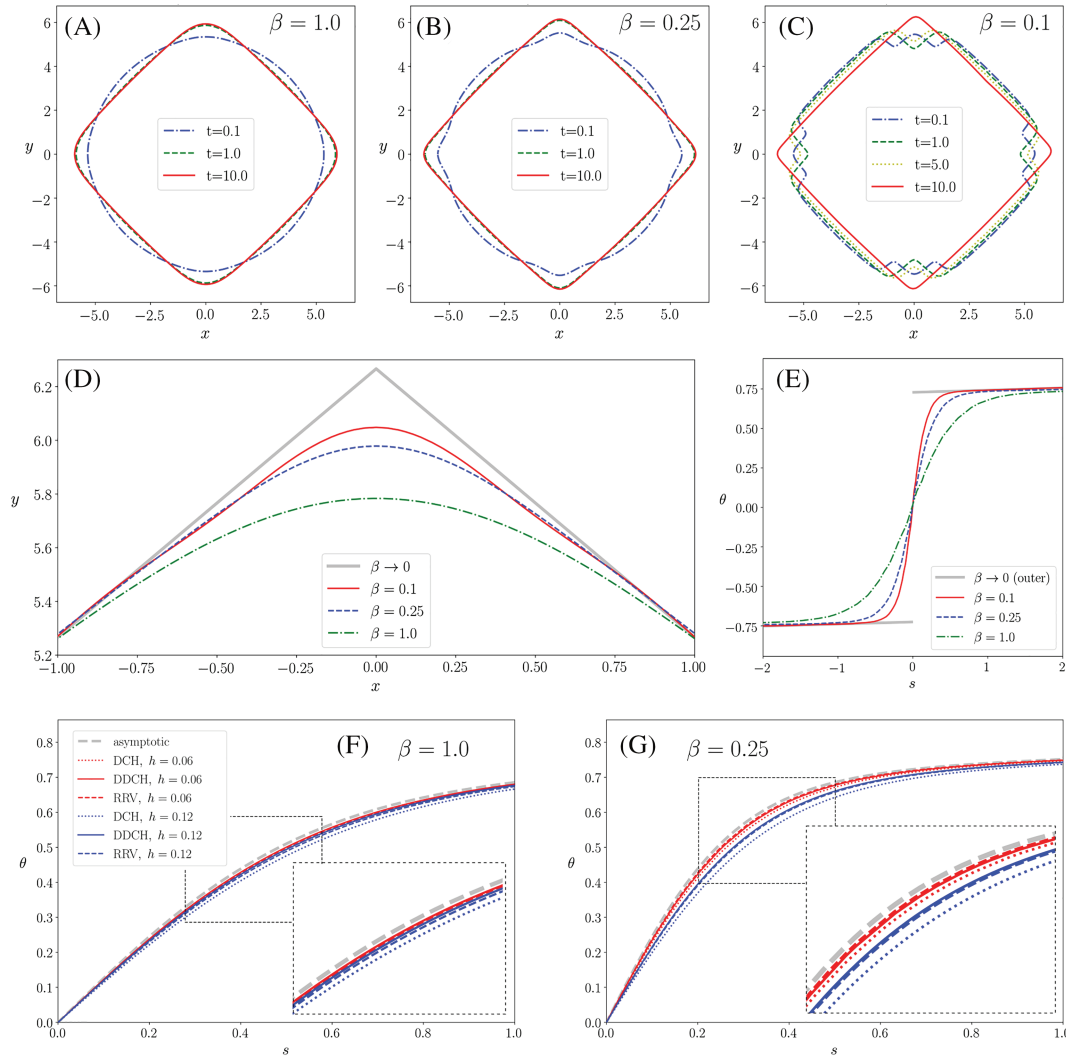
FIGURE 3 Analysis of faceting and corner rounding. Evolutions from a circle with radius 5 ($\varepsilon = 0.6$) to equilibrium with anisotropy as in Equation (24) with $C = \frac{1}{2}$: (A) $\beta = 1.0$, (B) $\beta = 0.25$, and (C) $\beta = 0.1$. The solutions are independent to further mesh refinement. Comparison of corner rounding in corresponding Wulff shape of limiting sharp interface problem if $\varepsilon \to 0$ for different β. Shown is the upper corner in (x,y) plot (D), and orientation θ as function of the arclength s (E). Comparison of $\theta(s)$ close to the corner obtained by the variational doubly degenerate Cahn–Hilliard (DDCH), RRV, and degenerate Cahn–Hilliard (DCH) models for two spatial discretizations for $\beta = 1.0$ (F) and $\beta = 0.25$ (G). The legend in (F) also holds for (G) [Colour figure can be viewed at wileyonlinelibrary.com]

possibility to specify anisotropies for a huge class of materials. Notice that with $\omega = 4$, $\rho_i = \bar{\rho}$, $\gamma_0 = 1$, and $\mathbf{m}_i = \pm \mathbf{e}_i$, this form for $\gamma(\hat{\mathbf{n}})$ corresponds to another well-known fourfold surface-energy function,

$$\gamma_4(\hat{\mathbf{n}}) = 1 - \bar{\rho}\left(n_x^4 + n_y^4 + n_z^4\right). \tag{27}$$

An example of faceting of a sphere in a strong anisotropy regime is shown in Figure 4. Therein, a surface-energy density with minima along {111} and {100} directions has been considered (see parameters in the caption). The shape corresponding to the isosurface $u = \frac{1}{2}$ is shown (panel A), along with the z-component of $\hat{\mathbf{n}}$ and $\gamma(\hat{\mathbf{n}})$ at the same isosurface (panels B and C, respectively), highlighting the facets along with the rounded edges and corners.

The faceting of a more complex shape is shown in Figure 5. We considered the *Stanford bunny*[57] (Figure 5A). The same surface-energy anisotropy as in Figure 4 with $\beta = 2 \cdot 10^{-4}$ is considered in Figure 5B–D, illustrating the $u = \frac{1}{2}$ isosurface, the z-component of $\hat{\mathbf{n}}$ and $\gamma(\hat{\mathbf{n}})$ after several time steps, respectively. Figure 5E–F shows the corresponding solution for different anisotropies. The parameters are set to reproduce the main facets of Si and GaAs crystals, respectively. The parameters considered for Si crystals: $\mathbf{m}_i = \{\langle 001 \rangle, \langle 111 \rangle, \langle 110 \rangle, \langle 113 \rangle\}$, $2\omega_{\langle 001 \rangle} = 2\omega_{\langle 111 \rangle} = 2\omega_{\langle 110 \rangle} = \omega_{\langle 113 \rangle} = 100$;
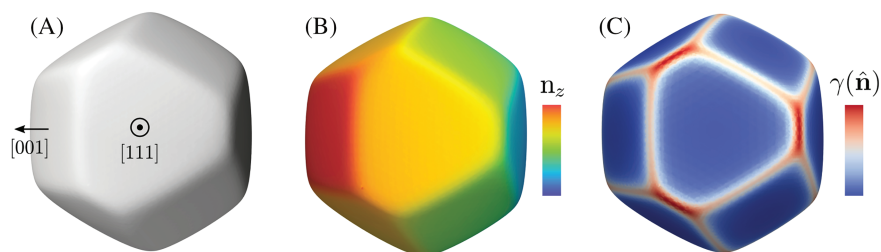
FIGURE 4 Equilibrium crystal shape obtained with the variational DDCH model. The initial configuration is a sphere with radius 1 ($\varepsilon = 0.2$). $\gamma(\hat{\mathbf{n}})$ as in Equation (26) with $\mathbf{m}_i$ corresponding to $\langle 001 \rangle$ and $\langle 111 \rangle$ directions, $\gamma_0 = 1$, $\rho_i = 0.3$, $\omega_i = 10$, and $\beta = 0.005$. (A) Isosurface $u = \frac{1}{2}$. (B) z-component of $\hat{\mathbf{n}}$, highlighting the formation of preferential orientations. (C) $\gamma(\hat{\mathbf{n}})$ [Colour figure can be viewed at wileyonlinelibrary.com]
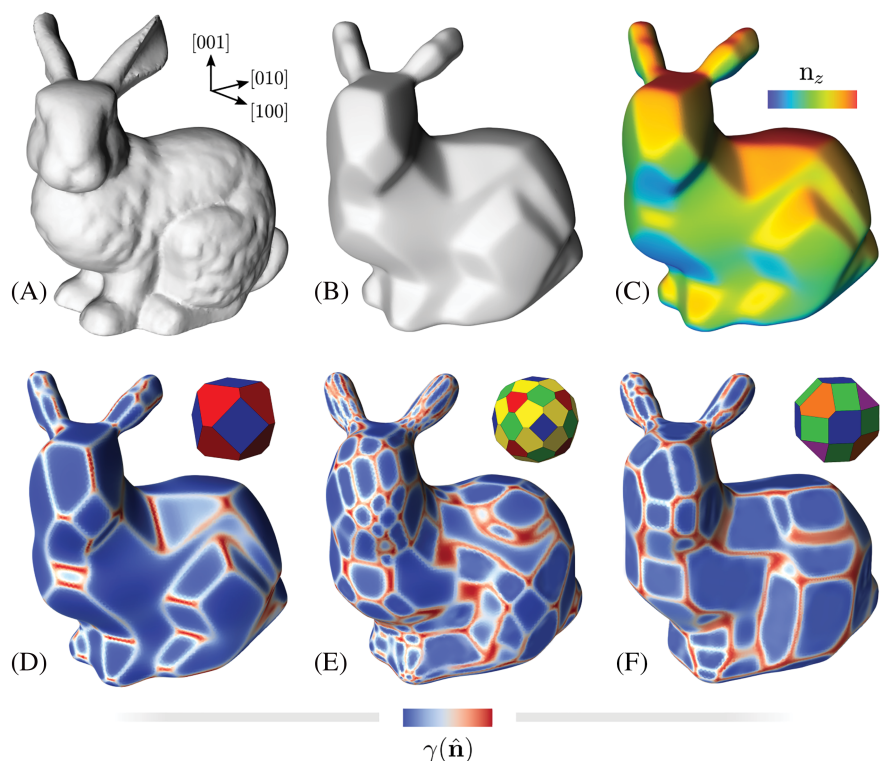

FIGURE 5 Faceting of the Stanford Bunny[57] by the DDCH model. The computational domain with size $1 \times 1 \times 1$ ($\varepsilon = 0.1$). (A) Initial condition (isosurface $u = \frac{1}{2}$); (B) faceted geometry after several time steps with anisotropy as in Figure 4 with $\beta = 2 \cdot 10^{-4}$; (C) z-component of $\hat{\mathbf{n}}$; (D) $\gamma(\hat{\mathbf{n}})$; (E) faceted geometry, illustrated by $\gamma(\hat{\mathbf{n}})$, obtained with a surface-energy anisotropy parametrization as for Si crystals with $\beta = 3 \cdot 10^{-4}$; and (F) as for GaAs crystals with $\beta = 3 \cdot 10^{-4}$. The Wulff shape (without edge and corner rounding) corresponding to anisotropies of panels (D)–(F) is also reported therein for comparison [Colour figure can be viewed at wileyonlinelibrary.com]

$\rho_{\langle 001 \rangle} = 0.08$, $\rho_{\langle 111 \rangle} = 0.07$, $\rho_{\langle 110 \rangle} = 0.07$ $\rho_{\langle 113 \rangle} = 0.075$ (qualitatively reproducing energetics as in Gai et al[58]), and for GaAs crystals: $\mathbf{m}_i = \{\langle 001 \rangle, \langle 111 \rangle, \langle 110 \rangle\}$, $\omega_{\langle 001 \rangle} = \omega_{\langle 111 \rangle} = \omega_{\langle 110 \rangle} = 50$, $\rho_{\langle 001 \rangle} = 0.1$, $\rho_{\langle 111A \rangle} = 0.06$, $\rho_{\langle 111B \rangle} = 0.12$ $\rho_{\langle 110 \rangle} = 0.12$ (qualitatively reproducing energetics as in Moll et al,[59] neglecting {113} facets). See also Salvalaglio et al.[28,33]

The nominal equilibrium crystal shapes, without corner rounding induced by the Willmore regularization, are reported in the upper right corners of Figure 5D–F for comparison. Notice that the shapes obtained in Figure 5 are not stationary. They show the solution at one time instance of the evolution, depicted to visualize the faceting of the initial condition. To comment on the positivity preserving property of the variational DDCH model, we have computed the average values for $-\min(u)$ and $\max(u) - 1$ over all simulations in Figure 5. We obtain the respective values $(1.1 \pm 0.4) \cdot 10^{-5}$ and $(0.8 \pm 0.3) \cdot 10^{-5}$, which are a bit larger than those exhibited in Figure 2 but still within the range of the *RRV model* in Figure 2. This deviation is expected to be larger in the 3D setting.

As a last example, we demonstrate the possibility to simulate coarsening of bulk nanoporous materials, as for example, considered with $\gamma(\hat{\mathbf{n}}) = 1$ in Geslin et al[31] and Andrews et al,[36] in a strongly anisotropic setting. We highlight a design project for the Digital Archive of Mathematical Models (DAMM).[60] Within computational domains, defined by the Wulff shapes, a classical Cahn–Hilliard model with random perturbations of $u = \frac{1}{2}$ as initial condition, is solved. After spinodal decomposition, the solution is used as initial condition for the anisotropic variational DDCH model, which is solved for several time steps similarly to Figure 5. The isosurface $u = \frac{1}{2}$ is extracted, postprocessed, and 3D printed. Figure 6 shows three examples of the resulting objects, a sphere (isotropic) and a cube and a tetrahedra with rounded corners and edges.

FIGURE 6 Objects are part of the Digital Archive of Mathematical Models (DAMM),[60] computed using AMDiS[52,53] by R. Backofen and F. Stenger, 3D print by materialise.com, photo by D. Lordick. Surface-energy anisotropies are set by Equation (26). (A) corresponds to the isotropic setting. (B) and (C) encode a cubic faceting with $\mathbf{m}_i = \pm\mathbf{e}_i$ and a tetrahedral faceting with $\mathbf{m}_1 = [\bar{1}\bar{1}\bar{1}]$, $\mathbf{m}_2 = [11\bar{1}]$, $\mathbf{m}_3 = [1\bar{1}1]$, $\mathbf{m}_4 = [\bar{1}11]$, respectively. For both the anisotropic cases, parameters are $\omega_i = 6$, $\rho_i = 0.9$, $\gamma_0 = 1$, and $\beta = 0.001$ [Colour figure can be viewed at wileyonlinelibrary.com]

(A)　　　(B)　　　(C)
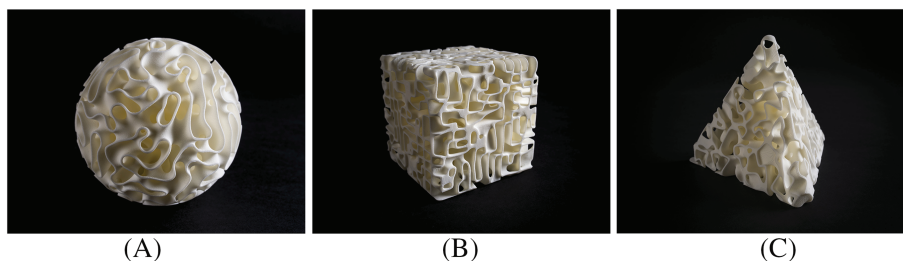
5 | CONCLUSIONS

In this paper, we have extended the variational DDCH model for isotropic surface diffusion[39] to the anisotropic case. We consider weak and strong anisotropies. The first case only requires the energy with a singular restriction function to be multiplied by a surface energy $\gamma(\hat{\mathbf{n}})$, as in Torabi et al.[14] The second case requires an additional regularization by a Willmore functional, again following Torabi et al.[14] A direct connection of the resulting models with the well known, and well used, nonvariational *RRV model*,[12] as possible in the isotropic case, cannot be achieved for anisotropic surface energies. However, numerical comparisons show the similarities of both approaches in terms of approximation properties to the sharp interface limit. We omit the asymptotic analysis of the anisotropic variation DDCH model. Formal convergence results to anisotropic surface diffusion can be obtained by combining the analysis in other studies. [12,14,39]

The slightly more complex variational DDCH models, if compared with the nonvariational *RRV model*,[12] not only gives energy dissipation and a mathematical foundation for numerical analysis but also provides better positivity preserving properties. Besides the superior approximations properties, this positivity preserving property enables the wide applicability of the model in Rätz et al[12] for large-scale applications. Our numerical results indicate that this property is further improved in the variational DDCH models. This is beneficial for several reasons. For a numerical point of view, it allows to optimize criteria based on thresholds or changes of u as, for example, for refining spatial discretization or adaptive timestepping. Also, these models are often coupled with additional equations in the bulk phases, which are characterized by the limiting values of u, for example, elasticity[12,33] or compositions.[37] In these cases, any improvement on positivity preservation, leads to increased accuracy.

However, besides these advantages, which will further foster to application of these models in materials science, as for the isotropic setting, several questions related to existence, uniqueness, and regularity of solutions, as well as to the positivity preserving property, remain open and need to be addressed.

CONFLICTS OF INTEREST

The authors certify that they have no affiliations with or involvement in any organization or entity with any financial or nonfinancial interest in the subject matter discussed in this manuscript.

ORCID

Marco Salvalaglio 🆔 https://orcid.org/0000-0002-4217-0951
Maximilian Selch 🆔 https://orcid.org/0000-0001-5586-6432
Axel Voigt 🆔 https://orcid.org/0000-0003-2564-3697
Steven M. Wise 🆔 https://orcid.org/0000-0003-3824-2075

REFERENCES

1. Mullins WW. Flattening of a nearly plane solid surface due to capillarity. *J Appl Phys*. 1959;30(1):77-83.
2. Cahn JW, Hoffman DW. A vector thermodynamics for anisotropic surfaces. *Acta Metall*. 1974;22:1205.
3. Bänsch E, Morin P, Nochetto RH. A finite element method for surface diffusion: the parametric case. *J Comput Phys*. 2005;203:321-343.
4. Haußer F, Voigt A. A discrete scheme for regularized anisotropic surface diffusion: a 6th order geometric evolution equation. *Interf Free Bound*. 2005;7:353-369.
5. Haußer F, Voigt A. A discrete scheme for parametric anisotropic surface diffusion. *J Sci Comput*. 2007;30(2):223-235.
6. Barrett JW, Garcke H, Nürnberg R. Numerical approximation of anisotropic geometric evolution equations in the plane. *Numer Math*. 2008;109:1-44.
7. Bao W, Jiang W, Wang Y, Zhao Q. A parametric finite element method for solid-state dewetting problems with anisotropic surface energies. *J Comput Phys*. 2017;330:380-400.
8. Barrett JW, Garcke H, Nürnberg R. Finite element methods for fourth order axisymmetric geometric evolution equations. *J Comput Phys*. 2019;376:733-766.
9. Cheng K, Wang C, Wise SM. A weakly nonlinear, energy stable scheme for the strongly anisotropic Cahn-Hilliard equation and its convergence analysis. *J Comput Phys*. 2020;405:109109.
10. Wise SM, Kim JS, Lowengrub JS. Solving the regularized, strongly anisotropic Cahn-Hilliard equation by an adaptive nonlinear multigrid method. *J Comput Phys*. 2007;226:414-446.
11. Wise SM, Lowengrub JS, Kim JS, Thornton K, Voorhees PW, Johnson WC. Quantum dot formation on a strain-patterned epitaxial thin film. *Appl Phys Lett*. 2005;87(13):133102.
12. Rätz A, Ribalta A, Voigt A. Surface evolution of elastically stressed films under deposition by a diffuse interface model. *J Comput Phys*. 2006;214(1):187-208.
13. Yeon D-H, Cha P-R, Grant M. Phase field model of stress-induced surface instabilities: surface diffusion. *Acta Mater*. 2006;54(6):1623-1630.
14. Torabi S, Lowengrub J, Voigt A, Wise S. A new phase-field model for strongly anisotropic systems. *Proc R Soc A*. 2009;465:1337-1359.
15. Li B, Lowengrub J, Rätz A, Voigt A. Geometric evolution laws for thin crystalline films: modeling and numerics. *Commun Comput Phys*. 2009;6(3):433.
16. Baňas L, Nürnberg R. Phase field computations for surface diffusion and void electromigration in $\mathbb{R}^3$. *Comput Vis Sci*. 2009;12(7):319-327.
17. Jiang W, Bao W, Thompson CV, Srolovitz DJ. Phase field approach for simulating solid-state dewetting problems. *Acta Mater*. 2012;60(15):5578-5592.
18. Salvalaglio M, Backofen R, Bergamaschini R, Montalenti F, Voigt A. Faceting of equilibrium and metastable nanostructures: a phase-field model of surface diffusion tackling realistic shapes. *Crys Growth Des*. 2015;15:2787-2794.
19. Bergamaschini R, Salvalaglio M, Backofen R, Voigt A, Montalenti F. Continuum modelling of semiconductor heteroepitaxy: an applied perspective. *Adv Phys X*. 2016;1(3):331-367.
20. Schiedung R, Kamachali RD, Steinbach I, Varnik F. Multi-phase-field model for surface and phase-boundary diffusion. *Phys Rev E*. 2017;96:012801.
21. Cahn JW, Elliott CM, Novick-Cohen A. The Cahn-Hilliard equation with a concentration dependent mobility: motion by minus the Laplacian of the mean curvature. *Euro J Appl Math*. 1996;7:287-301.
22. Gugenberger C, Spatschek R, Kassner K. Comparison of phase-field models for surface diffusion. *Phys Rev E*. 2008;78:016703.
23. Dziwnik M, Münch A, Wagner A. An anisotropic phase-field model for solid-state dewetting and its sharp-interface limit. *Nonlinearity*. 2017;30:1465-1496.
24. Karma A, Rappel W-J. Quantitative phase-field modeling of dendritic growth in two and three dimensions. *Phys Rev E*. 1998;57:4323-4349.
25. Backofen R, Wise SM, Salvalaglio M, Voigt A. Convexity splitting in a phase field model for surface diffusion. *Int J Num Anal Mod*. 2019;16(2):192-209.
26. Albani M, Bergamaschini R, Montalenti F. Dynamics of pit filling in heteroepitaxy via phase-field simulations. *Phys Rev B*. 2016;94(7):075303.
27. Salvalaglio M, Bergamaschini R, Isa F, et al. Engineered coalescence by annealing 3D Ge microstructures into high-quality suspended layers on Si. *ACS Appl Mater Interf*. 2015;7(34):19219-19225.
28. Salvalaglio M, Bergamaschini R, Backofen R, Voigt A, Montalenti F, Miglio L. Phase-field simulations of faceted Ge/Si-crystal arrays, merging into a suspended film. *Appl Surf Sci*. 2017;391:33-38.
29. Salvalaglio M, Backofen R, Voigt A, Montalenti F. Morphological evolution of pit-patterned Si(001) substrates driven by surface-energy reduction. *Nanoscale Res Lett*. 2017;12(1):554.

30. Naffouti M, Backofen R, Salvalaglio M, et al. Complex dewetting scenarios of ultrathin silicon films for large-scale nanoarchitectures. *Sci Adv*. 2017;3(11):eaao1472.

31. Geslin P-A, Buchet M, Wada T, Kato H. Phase-field investigation of the coarsening of porous structures by surface diffusion. *Phys Rev Mater*. 2019;3:083401.

32. Albani M, Ghisalberti L, Bergamaschini R, et al. Growth kinetics and morphological analysis of homoepitaxial GaAs fins by theory and experiment. *Phys Rev Mater*. 2018;2(9):093404.

33. Salvalaglio M, Zaumseil P, Yamamoto Y, et al. Morphological evolution of Ge/Si nano-strips driven by Rayleigh-like instability. *Appl Phys Lett*. 2018;112(2):022101.

34. Albani M, Bergamaschini R, Salvalaglio M, Voigt A, Miglio L, Montalenti F. Competition between kinetics and thermodynamics during the growth of faceted crystal by phase field modeling. *Phys Status Solidi (b)*. 2019;256(7):1800518.

35. Bollani M, Salvalaglio M, Benali A, et al. Templated dewetting of single-crystal sub-millimeter-long nanowires and on-chip silicon circuits. *Nat Commun*. 2019;10(1):5632.

36. Andrews WB, Elder KLM, Voorhees PW, Thornton K. Coarsening of bicontinuous microstructures via surface diffusion. *Phys Rev Mater*. 2020;4:103401.

37. Bergamaschini R, Montalenti F, Miglio L. Sunburst pattern by kinetic segregation in core-shell nanowires: a phase-field study. *Appl Surf Sci*. 2020;517:146056.

38. Salvalaglio M, Bouabdellaoui M, Bollani M, et al. Hyperuniform monocrystalline structures by spinodal solid-state dewetting. *Phys Rev Lett*. 2020;125:126101.

39. Salvalaglio M, Voigt A, Wise S. Doubly degenerate diffuse interface models of surface diffusion. *Math Method Appl Sci*. 2021;44.

40. Kobayashi R. Modeling and numerical simulations of dendritic crystal growth. *Physica D*. 1993;63(3-4):410-423.

41. Barrett JW, Garcke H, Nürnberg R. On the stable discretization of strongly anisotropic phase field models with applications to crystal growth. *Z Angew Math Mech*. 2013;93:717-732.

42. Barrett JW, Garcke H, Nürnberg R. Stable phase field approximations of anisotropic solidification. *IMA J Numer Anal*. 2014;34:1289-1327.

43. Gurtin ME, Jabbour ME. Interface evolution in three dimensions with curvature-dependent energy and surface diffusion: interface-controlled evolution, phase transitions, epitaxial growth of elastic films. *Arch Rat Mech Anal*. 2002;163:171-208.

44. De Giorgi E. *Some Remarks on Γ-Convergence and Least Squares Method*. Boston, MA: Birkhäuser Boston; 1991;135-142.

45. Loreti P, March R. Propagation of fronts in a nonlinear fourth order equation. *European J Appl Math*. 2000;11:203-213.

46. Du Q, Liu C, Ryham R, Wang X. A phase field formulation of the Willmore problem. *Nonlinearity*. 2005;18(3):1249-1267.

47. Röger M, Schätzle R. On a modified conjecture of De Giorgi. *Math Z*. 2006;254:675-714.

48. Dai S, Du Q. Coarsening mechanism for systems governed by the Cahn-Hilliard equation with degenerate diffusion mobility. *Multisc Model Simul*. 2014;12:1870-1889.

49. Lee AA, Münsch A, Süli E. Degenerate mobilities in phase field models are insufficient to capture surface diffusion. *Appl Phys Lett*. 2015;107:081603.

50. Lee AA, Münsch A, Süli E. Sharp-interface limits of the Cahn-Hilliard equation with degenerate mobility. *SIAM J Appl Math*. 2016;76:433-456.

51. Voigt A. Comment on "Degenerate mobilities in phase field models are insufficient to capture surface diffusion" [Appl. Phys. Lett. 107, 081603 (2015)]. *Appl Phys Lett*. 2016;108(3):036101.

52. Vey S, Voigt A. AMDiS: adaptive multidimensional simulations. *Comput Visual Sci*. 2007;10(1):57-67. English.

53. Witkowski T, Ling S, Praetorius S, Voigt A. Software concepts and numerical algorithms for a scalable adaptive parallel finite element method. *Adv Comput Math*. 2015;41:1145.

54. van der Vorst HA. Bi-CGSTAB: a fast and smoothly converging variant of bi-CG for the solution of nonsymmetric linear systems. *SIAM J Sci Comput*. 1992;13(2):631-644.

55. Davis TA. A column pre-ordering strategy for the unsymmetric-pattern multifrontal method. *ACM Trans Math Softw*. 2004;30(2):196-199.

56. Spencer BJ. Asymptotic solutions for the equilibrium crystal shape with small corner energy regularization. *Phys Rev E*. 2004;69:011603.

57. Turk M. The Stanford Bunny, https://www.cc.gatech.edu/turk/bunny/bunny.html.

58. Gai Z, Yang W, Zhao R, Sakurai T. Macroscopic and nanoscale faceting of germanium surfaces. *Phys Rev B*. 1999;59(23):15230-15239.

59. Moll N, Kley A, Pehlke E, Scheffler M. Gaas equilibrium crystal shape from first principles. *Phys Rev B*. 1996;54:8844-8855.

60. Digital Archive of Mathematical Models (DAMM). https://mathematical-models.org